only because some marine terraces are evidently capped by corals belonging to more than one interglacial stage and the precision of the ESR dates is estimated at ±15%. In addition, uplift rates may not have remained constant in time. Nevertheless, a check was made to discover whether a constant uplift rate could be found that would be consistent with most of the data available. Only unequivocal sea-level indicators, such as reef crests and notches, were used for correlation. Graphic attempts were made to find empirically whether a series of parallel uplift lines existed that would project past high sea levels, deduced from O isotope data and plotted with uncertainty ranges in Fig. 2A, into the vertical uncertainty ranges of sea-level indicators along the reference transect. The "best fitting" uplift rate is 0.49 ± 0.01 mm/year. At this rate, the elevation of the upper terrace (VI_2) corresponds to the superimposed effect of stages 27 and 29 and is therefore about 1 million years old. At the same uplift rate, most terrace elevations are consistent with certain interglacial stages (VI_1 with stage 25, V_2 with stage 23, V_1 with stage 21, V_0 and IV_3 with stage 19, IV_2 with stage 17; IV_1 is dated at stage 15; III_3 is consistent with stage 13, III_2 with stage 11; III_1 is dated at stage 9; the lower parts of II_5 and II_4 correspond to stage 7; II_3 was dated at stages 9 and 7 but was probably at sea level also during stage 5e; II_2 was dated at stages 7 and 5). Although the sea-level curve since 250 ka (Fig. 2B) may still be uncertain in some parts and slightly different from curves proposed by other investigators, it shows clearly that at an uplift rate of 0.5 mm/year superimposition of marine effects of different ages may occur at similar elevations.

In conclusion, Sumba Island terraces represent one of the longest series for mid-Pleistocene times. The close correlation between the raised marine sequence and the revised O isotope chronology (*16*) supports the reliability of this chronology for Quaternary studies. It also suggests that sea level was probably near to its present level at the maximum of stages 13 and 15 (O isotope values lower than the Holocene ones at these stages may be attributable to colder oceanic deep waters), possibly at −20 ± 10 m at stage 17, at −15 ± 10 m at stage 19, and between −25 and −40 m at stage 23.

ESR can be used to date older samples than α- or mass spectroscopy U-dating and is therefore the only tool that can be used today for a direct dating of mid- and early Pleistocene reef tracts. However, ESR is not precise enough to distinguish between interstadial substages. The spectacular sequence of marine terraces on Sumba Island make this an exceptionally favorable place to carry out new studies on the chemical, physical, isotopic, morphological, ecological, paleoclimatic, pedological, and diagenetic changes that have occurred during the past million years.

REFERENCES AND NOTES

1. J. Chappell, *Geol. Soc. Am. Bull.* **85**, 553 (1974); A. L. Bloom *et al. Quat. Res.* **4**, 185 (1974).
2. 1 ka = 1000 years ago.
3. J. Chappell and N. J. Shackleton, *Nature* **324**, 137 (1986).
4. K. J. Mesolella, R. K. Matthews, W. S. Broecker, D. L. Thurber, *J. Geol.* **77**, 250 (1969).
5. M. L. Bender *et al.*, *Geol. Soc. Am. Bull.* **90**, 577 (1979).
6. M. Ikeya, *Nature* **255**, 48 (1975).
7. U. Radtke, R. Grün, P. Schwarcz, *Quat. Res. (N.Y.)* **29**, 197 (1988).
8. R. L. Edwards, J. H. Chen, T.-L. Ku, G. J. Wasserburg, *Science* **236**, 1547 (1987).
9. J. Chappell and H. H. Veeh, *Geol. Soc. Am. Bull.* **89**, 356 (1978).
10. C. Jouannic *et al.*, *Proc. 6th Int. Coral Reef Symp., Australia*, **3**, 441 (1988); W. S. Hantoro, C. Jouannic, P. A. Pirazzoli, *Photo Interprét.* **89** (no. 1), 17 (1989).
11. L. F. Montaggioni and C. T. Hoang, *Palaeogeogr. Palaeoclimatol. Palaeoecol.* **64**, 79 (1988); C. Causse and C. Hillaire-Marcel, in *Initial Reports, Ocean Drilling Program, B*, S. K. Stewart, Ed. (Government Printing Office, Washington, DC, 1989), pp. 551–560.
12. R. Grün, *Quat. Int.* **1**, 66 (1989).
13. _____ *et al.*, *Quat. Sci. Rev.*, in press.
14. Elevations, related to mean sea level, correspond to the upper surface of former reef crests along the reference transect.
15. J. Imbrie *et al.*, *North Atlantic Treaty Organization Adv. Study Inst. Ser. C* **126** (no. 1), 269 (1984).
16. N. J. Shackleton, A. Berger, W. R. Peltier, *Trans. R. Soc. Edinburgh Earth Sci.* **81**, 251 (1990).
17. N. J. Shackleton, *Quat. Sci. Rev.* **6**, 183 (1987).

20 December 1990; accepted 17 April 1991

Development of Diapiric Structures in the Upper Mantle Due to Phase Transitions

M. LIU, D. A. YUEN, W. ZHAO, S. HONDA

Solid-state phase transitions in time-dependent mantle convection can induce diapiric flows in the upper mantle. When a deep mantle plume rises toward phase boundaries in the upper mantle, the changes in the local thermal buoyancy, local heat capacity, and latent heat associated with the phase change at a depth of 670 kilometers tend to pinch off the plume head from the feeding stem and form a diapir. This mechanism may explain episodic hot spot volcanism. The nature of the multiple phase boundaries at the boundary between the upper and lower mantle may control the fate of deep mantle plumes, allowing hot plumes to go through and retarding the tepid ones.

ONE OF THE STRIKING FEATURES ON the earth's surface is linear volcanic islands, such as the Hawaiian-Emperor chain in the Pacific. Morgan suggested (*1*) that these volcanic lineations were formed when plates move over relatively stationary hot regions, called hot spots, which are thought to result from deep mantle plumes.

An important feature of hot spot volcanism is the nature of the episodic eruptions and their role in the formation of discrete volcanoes along the chain. This manifestation suggests that mantle plumes are in the form of diapirs instead of continuous conduits. Such a notion is supported in part by surface wave studies from seismic tomography, which have found no continuous thermal anomalies at a depth of 300 km under the Hawaiian Islands (*2*).

M. Liu, Department of Geosciences, Pennsylvania State University, University Park, PA 16802.
D. A. Yuen and W. Zhao, Minnesota Supercomputer Institute and Department of Geology and Geophysics, University of Minnesota, Minneapolis, MN 55455.
S. Honda, Institute of Geology, Hiroshima University, 730 Hiroshima, Japan.

Some fluid dynamical mechanisms have been proposed to explain the generation of mantle diapirs. Deep mantle plumes may be sheared off by large-scale background circulation (*3*). Solitary wave disturbances (*4*) propagating within "mantle conduits" may also cause time-dependent plume behavior. In this report we describe mantle diapirs generated by the interaction between deep mantle plumes and polymorphic solid-state phase transitions in the upper mantle. Although temperature-dependent viscosity may be influential in mantle convection, other mechanisms, such as the effects of phase transitions on plumes, may also be important.

There are various mineral assemblages in the transition zone between depths of 350 and 700 km. Recent theoretical (*5*) and experimental (*6, 7*) work has established the major phase boundaries in the transition zone. Diapiric flows may be generated from the interaction of mantle flows with solid-solid phase transitions (*8*). These diapirs, which are isolated rising thermal anomalies, are generated from a rising plume as a result of changes in the local buoyancy, local heat

capacity, and latent heat associated with phase transitions.

We have developed here a formalism in which the effects of phase transitions can be incorporated more easily than in the previous convection models (*9*). We use a two-dimensional Gaussian distribution $f(T,p)$ over the nondimensional T (temperature) and p (pressure) space to describe the location of a phase change (see Table 1). For any segment of an equilibrium phase boundary, which is governed by Clausius-Clapeyron slope γ, we may express the phase distribution function as

$$f(T, p) = \exp[-(\gamma T - p + p_0)^2]/\tau^2 \quad (1)$$

Here P_0 is the pressure intercept and τ is the dimensionless pressure width of the Gaussian peak used to control the thickness of the transition zone. The equation of a phase boundary segment is given by $p = p_0 + \gamma T$. This Gaussian function portrays the location of the phase-transition zone, which normally has a width less than 10 km. This approach also allows for the treatment of invariant points (for example, triple points) in phase diagram where several phase segments would meet. Using this phase distribution function, we can generalize this approach to multiple phase transitions to account for the enhanced effects on local buoyancy, expressed in terms of an effective thermal expansivity α (*10*), an effective heat capacity C_p (*10*), and latent heat release ΔH_i, where i represents an individual phase:

$$\alpha(T, p) = \alpha_0(p)\left(1 + \sum_{i=1}^{k} \frac{\Delta\rho f_i}{\rho_0 \delta T}\right) \quad (2)$$

$$C_p(T, p) = C_p\left(1 + \sum_{i=1}^{k} \frac{\Delta H_i f_i}{C_p \delta T}\right) \quad (3)$$

$$\Delta H_i = \frac{\gamma_i T \Delta\rho_i}{\rho_0^2} \quad (4)$$

where ρ_0 is the background mantle density and $\Delta\rho_i$ is the density change. The temperature interval over which the phase change takes place is given by δT. The background thermal expansivity $\alpha_0(p)$ decreases as a function of depth in accordance with recent laboratory findings (*11*). The functional dependence is parameterized by an algebraic power-law dependence with depth (*12*). The index k represents the number of phase transition segments considered.

We will use the extended-Boussinesq approximation to study the problem of plumes interacting with mantle phase transitions. This approximation enables us to handle multiple phase transitions in conjunction with a triple point much more easily than in the case in which the effects of background density stratification (*13*) are included. The dimensionless momentum equation in the stream-function-vorticity (Ψ,ω) formulation is

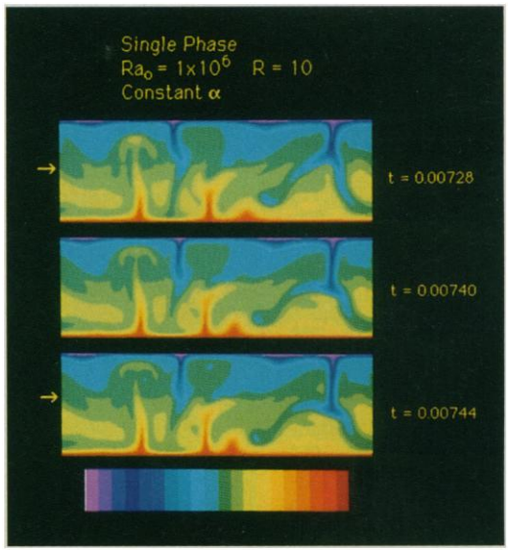

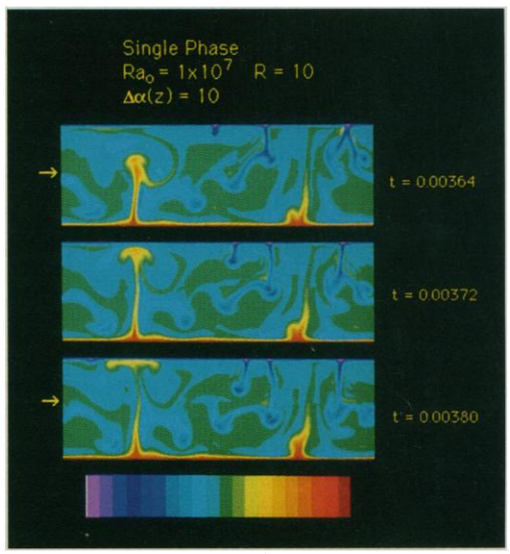

Fig. 1 (**top**). Development of a mantle diapir at the phase boundary near a depth of 670 km. Only the post-spinel to perovskite phase boundary is considered with a Clapeyron slope of -2.6 MPa K^{-1}. A constant thermal expansivity is used in this partially internally heated ($R = 10$) system with $Ra = 10^6$. Time t is nondimensionalized with respect to thermal diffusion time (see Table 1). These are sequential snapshots taken after five overturns. The arrow on the side denotes a depth of 670 km. Notice the mantle diapir developed from the hot plume on the left. Color scale: light purple ($T = 0$) to dark red ($T = 1$). Contour level is 0.05. $T = 0.5$ is between the yellow-green and light blue. **Fig. 2.** (**middle**). Same as in Fig. 1 except for the presence of depth-dependent thermal expansivity; $\alpha(z)$ decreases by a factor of 10 across the layer according to an analytical formula (*9*). The surface Ra is 10^7, and the averaged Ra is 3×10^6. Arrow denotes a depth of 670 km. **Fig. 3.** (**bottom**). Development of a mantle plume with multiple phase transitions and a triple point. Compared with Figs. 1 and 2, in this figure three more phase boundaries are added in the model. The first is the transition from olivine to β-spinel with $\gamma = 3.6$ GPa K^{-1}; the second is the transition from β-spinel to γ-spinel at a depth of 550 km with a slope of 11 GPa K^{-1}; the third is the nearly vertical branch (dT/dp around zero) extending from the triple point ($p = 22$ GPa and $T = 2000$ K) to the solidus curve. The two arrows denote, respectively, depths of 400 and 670 km. Values of the physical parameters $\alpha(z)$, R, and Ra_0 are the same as in Fig. 2. Notice how the left plume head (orange) impinges on the phase transition (first panel). It finally penetrates into the upper mantle (second panel), and the mushroom arrives at the surface with a very thin stem, less than 40 km wide (third panel). In contrast, the right plume, being cooler, cannot penetrate deeply into the upper mantle.

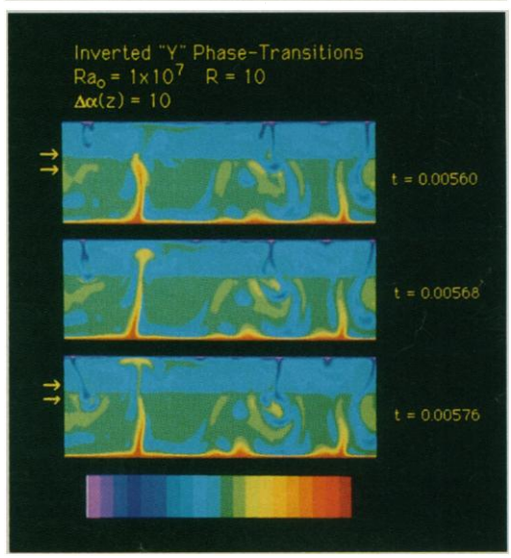

$$\nabla^2 2\omega = -Ra_0\alpha(T,z)\frac{\partial T}{\partial x} \quad (5)$$

where x and z are, respectively, dimensionless horizontal and vertical coordinates with the z axis pointing upward, and Ra_0 is the Rayleigh number based on the entire layer depth and the surface physical properties. The hydrostatic pressure has been converted to depth in $\alpha(T,z)$ in Eq. 5. The time-dependent energy equation takes the form

$$\frac{\partial T}{\partial t} = \frac{1}{C_p(T,z)}\left[\nabla^2 T + wD_0\alpha(T,z)(T+T_0) + R + \frac{D_0}{Ra_0}\tau_{ij}\frac{\partial u_i}{\partial x_j}\right] - \mathbf{u}\cdot\nabla T - \sum_{i=1}^{k}\frac{w\Delta H_i f_i}{\delta z} \quad (6)$$

where w is the vertical velocity, u_i is the velocity component, D_0 is the dissipation number (*14*) based on surface properties, τ_{ij} is the deviatoric stress tensor and δz is a characteristic width of a phase transition zone, T_0 is the nondimensional surface temperature, and R is the internal heating parameter (*15*) for a bottom-heated configuration.

Equations 5 and 6 include the effects of phase changes in the momentum equation and latent heat release in the energy equation. The equations are integrated in time by means of a finite-difference method (*16*). The boundary conditions at the top and bottom are constant temperature and stress-free. Periodic boundary conditions are used along the vertical edges. An equidistant grid consisting of 100 by 300 points is used for a model mantle that is scaled to be 1500 km deep and 4500 km wide. Solutions were checked with a 150 × 450 grid. The depths of the phase transitions lie between 400 and 670 km. A nearly chondritic mantle (R = 10) has been assumed. Other physical parameters are provided in Table 1.

For a simulation of the spinel-perovskite transition separating the upper and lower mantles (Fig. 1), diapiric structures develop in the upper mantle from the interaction between the plumes and the phase transition for Ra_0 of 10^6. All solutions shown have been integrated over for at least five overturns and are no longer in the initial transient regime. In this model we used a constant thermal expansivity and a slope γ of -2.6 MPa K^{-1} for the transition (*17*). This is a major phase transition (*19*) separating the upper mantle from the lower mantle for temperatures below about 2400 K (*5, 7*). In this model, however, γ has been extended (*8*) across the entire (T,p) plane, as in earlier work (*9, 13*).

When a hot mantle plume rises toward this phase boundary, it encounters resistance because of the phase boundary deflecting upward; this is caused by the negative Clapeyron slope interacting with the flow. However, in the phase-transition zone the deep mantle plume gains extra local buoyancy (see α in Eqs. 2 and 5) because of the decrease in density across the phase boundary and also extra heat release from the phase change. These factors provide an additional source of buoyancy. Once the plume head has penetrated the phase boundary, the boost from both enhanced thermal expansivity and latent heat accelerates it upward. All of these effects act to tear apart the plume head from the feeding stem of the plume and to form mantle diapirs. With time, these diapirs are pinched off at the phase transition region at $z = 0.55$ (shown by the arrow in Fig. 1). For thermal convection without phase transitions, disconnected plume structures are not observed at Ra = 10^6 but at much higher Ra in the regime of hard turbulent convection (*18*). In this numerical experiment we can observe that the separation of the plume head is facilitated by the phase transition. The temperature difference between the upper and lower mantles is between 50 and 70 K in this case, as can be seen by the changes in the color.

In the case of a depth-dependent α (Fig. 2), there is a gradual separation of plume heads from the phase boundary. The surface Ra for this case is 10^7 and the averaged Ra is 3×10^6. The plumes are thinner and faster (the time interval is the same in Figs. 1 and 2) in the case of depth-dependent α. Only the left plume with a larger thermal anomaly can penetrate and evolve into a mushroom structure; the right plume, being cooler, cannot fully develop in the upper mantle. Diapiric structures are formed much more easily for plumes with thinner stems (see bottom panel) than for those with thicker columns. These thin stems, less than 40 km wide, cannot be detected by seismic tomography with the use of surface waves (*2*). There is a small temperature difference of around 20 K between the upper and lower mantles.

The effects are more complicated (Fig. 3) when we include the multiple phase transitions associated with the triple point (*5, 7*) at a depth of 670 km and the transition from olivine to β-spinel (*18*) at a depth of 400 km. The multiple phase transitions take the form of an inverted letter "Y" with the juncture being the triple point located at around 670 km and between 2000 and 2400 K (*5, 7*). The two univariant branches represent, respectively, the positive slope for the transition from β-spinel to γ-spinel (*6, 20*) and the negative slope for the transition from γ-spinel to perovskite (*17*). The vertical branch with a nearly zero Clapeyron slope extends from the triple point up to the solidus curve (*5, 7*). The surface Ra and depth-dependent α were the same as in Fig. 2.

One striking effect of multiple phase transitions is the asymmetry in the dynamics between ascending and descending plumes. This is due to the particular layout of the upper mantle phase boundaries over the (T,p) plane. Ascending plumes with temperatures lower than the triple-point temperature (see the right plume in Fig. 3) would encounter more phase transitions with a shorter depth interval than the descending plumes (in blue). On the other hand, very hot plumes (see the left plume) can go through the flat Clapeyron-slope branch unimpeded. This process is further aided by the enhanced expansivity from the density decrease. The temperature field resembles that for layered convection, even though the flow field itself is not layered. There is a temperature drop of about 175 K across the transition zone.

Many other factors in the mantle can also influence the generation of diapirs. One of these is the depth dependence of thermal expansivity, which may decrease significantly through the mantle (*11*). We have studied the effects of depth-dependent α, using the dependence on depth given by Zhao and

Table 1. Model parameters.

Parameter	Description	Value
d	Depth of the layer	1500 km
ΔT	Temperature drop across the layer	2500 K
T_0	Temperature at the top of the layer	500 K
D_0	Dissipation number	0.3
ρ_0	Background mantle density	3500 kg m^{-3}
g	Gravitational acceleration	10 m s^{-2}
C_p	Background heat capacity	1 kJ kg^{-1} K^{-1}
R	Internal heating ratio	10
δz	Dimensionless thickness of phase transition	0.01 = 15 km
δT	Dimensionless temperature drop across phase transition	0.02 = 50 K
τ	Dimensionless width of Gaussian peak	0.01 = 1.05 GPa
t	Time nondimensionalized by thermal diffusion across the layer	0.001 = 71.6 Ma

Yuen (*12*). Recent studies by Leitch *et al.* (*21*) and Yuen *et al.* (*22*) have shown that the decrease of α with depth plays a significant role in deep mantle convection and results in steady hot plumes and in convection cells with large aspect ratios. For multiple phase changes, depth-dependent α may allow deep mantle plumes to break through the closely clustered phase transitions. Otherwise, deep mantle plumes might be confined to the lower mantle and layered convection would prevail (*9, 13*).

Internal heating from radioactive decay is another important factor that helps to produce mantle diapirs. All of the results we have shown in this report are calculated with $R = 10$, nearly the chondritic value. In other numerical experiments without internal heating ($R = 0$), we find that pure basal heating would produce very steady plumes. These plumes cannot as easily be torn up into mantle diapirs as plumes in internally heated systems. Temperature-dependent viscosity causes thinner and faster plumes, which are dynamically more susceptible to becoming diapirs. Likewise, three-dimensional geometry (*23*) would cause thinner cylindrical plumes (*24*), which are more likely to produce diapirs.

Phase transitions are not the only means for generating diapiric structures in the mantle. At higher *Ra*, between 10^7 and 10^8, diapirs (*18, 25*) are common in ordinary thermal convection. Phase transitions in the upper mantle can promote the generation of mantle diapirs at lower *Ra*, of order 10^6. This is a complicated phenomenon that warrants further investigation (*26*). These numerical simulations demonstrate that multiple phase transitions at the 670-km discontinuity can control the dynamics of plumes, in particular, by filtering out tepid deep-mantle plumes and preferentially concentrating hot plumes in the upper mantle. The diapiric flows (*27*), induced by phase transitions, may be important for understanding the episodic nature of hot-spot volcanism.

REFERENCES AND NOTES

1. W. J. Morgan, *Nature* **230**, 42 (1971).
2. Y. Zhang and T. Tanimoto, *Geophys. J. Int.* **98**, 255 (1989).
3. J. N. Skilbeck and J. A. Whitehead, *Nature* **272**, 499 (1978).
4. G. Schubert, P. L. Olson, C. Anderson, P. Goldman, *J. Geophys. Res.* **94**, 9623 (1989).
5. Y. Fei, S. K. Saxena, A. Navrotsky, *ibid.* **95**, 6915 (1990).
6. E. Ito and E. Takahashi, *ibid.* **94**, 10637 (1989).
7. R. Boehler, A. Chopelas, *Geophys. Res. Lett.*, in press.
8. D. L. Anderson, *J. Geophys. Res.* **92**, 13968 (1987).
9. U. R. Christensen and D. A. Yuen, *ibid.* **90**, 10291 (1985).
10. G. Schubert, D. A. Yuen, D. L. Turcotte, *Geophys. J. R. Astron. Soc.* **42**, 705 (1975).
11. A. Chopelas and R. Boehler, *Geophys. Res. Lett.* **16**, 1347 (1989).
12. W. Zhao and D. A. Yuen, *ibid.* **14**, 1223 (1987).
13. P. Machetel and P. Weber, *Nature* **350**, 55 (1991).
14. G. T. Jarvis and D. P. McKenzie, *J. Fluid Mech.* **96**, 515 (1980).
15. S. A. Weinstein, P. L. Olson, D. A. Yuen, *Geophys. Astrophys. Fluid. Dyn.* **47**, 157 (1989).
16. S. Honda and D. A. Yuen, *Earth Planet. Sci. Lett.* **99**, 349 (1990).
17. E. Ito *et al.*, *Science* **249**, 1275 (1990).
18. U. Hansen, D. A. Yuen, S. Kroening, *Phys. Fluids A* **2** (no. 12), 2157 (1990).
19. D. L. Anderson, *Science* **157**, 1165 (1967).
20. _____ and J. Bass, *Nature* **320**, 321 (1986).
21. A. M. Leitch, D. A. Yuen, G. Sewell, *Earth Planet. Sci. Lett.* **102**, 213 (1991).
22. D. A. Yuen *et al.*, in *Glacial Isostasy, Sealevel and Mantle Rheology*, R. Sabadini and K. Lambeck, Eds. (Kluwer Academic, Dordrecht, Holland, 1991), p. 663.
23. G. Houseman, *Nature* **332**, 346 (1988).
24. M. Liu and C. Chase, *Geophys. J. Int.* **100**, 433 (1991).
25. T. H. Solomon and J. P. Gollub, *Phys. Rev. Lett.* **64**, 2382 (1990).
26. Other factors that will influence the generation of diapirs from phase-transition boundaries are temperature-dependent viscosity, non-Newtonian rheology, and the possibility of a hard rheology in the transition zone [S. Karato, *Phys. Earth Planet. Inter.* **55**, 234 (1989)].
27. The diapirs at the base of the lithosphere are several hundred kilometers wide, as one can estimate from the distance between the two arrows in Fig. 3 (270 km). For this grid resolution and the pixels used in the visualization, the width of the discernible conduit associated with the left plume in the bottom panel of Fig. 3 is about 30 km.

28. We thank D. Anderson, R. Boehler, and A. Chopelas for helpful discussions and continual encouragement. Research supported by the National Aeronautics and Space Administration and initiated at Maxwell's. S. Roe's help is gratefully acknowledged. We are grateful to IBM Corporation for processor time on the IBM-3090-600J computer.

30 January 1991; accepted 22 April 1991

Regulation of B Cell Antigen Receptor Signal Transduction and Phosphorylation by CD45

LOUIS B. JUSTEMENT,* KERRY S. CAMPBELL, NADINE C. CHIEN, JOHN C. CAMBIER†

CD45 is a member of a family of membrane proteins that possess phosphotyrosine phosphatase activity, and is the source of much of the tyrosine phosphatase activity in lymphocytes. In view of its enzymatic activity and high copy number, it seems likely that CD45 functions in transmembrane signal transduction by lymphocyte receptors that are coupled to activation of tyrosine kinases. The B cell antigen receptor was found to transduce a Ca^{2+}-mobilizing signal only if cells expressed CD45. Also, both membrane immunoglobulin M (mIgM) and CD45 were lost from the surface of cells treated with antibody to CD45, suggesting a physical interaction between these proteins. Finally, CD45 dephosphorylated a complex of mIg-associated proteins that appears to function in signal transduction by the antigen receptor. These data indicate that CD45 occurs as a component of a complex of proteins associated with the antigen receptor, and that CD45 may regulate signal transduction by modulating the phosphorylation state of the antigen receptor subunits.

THE MEMBRANE GLYCOPROTEIN CD45 is a necessary participant in the regulation of signal transduction by a number of lymphocyte receptors. In both T and B cells, receptor-mediated generation of second messengers and changes in cellular activation can be modified by co–cross-linking of CD45 with these receptors, suggesting that CD45 may act as a common regulatory protein in lymphocytes (*1*). Direct evidence that CD45 is important for T cell activation has been provided by studies of CD4, CD8, and the T cell receptor:CD3 complex. CD45 regulates the phosphorylation state and activity of the tyrosine-specific kinase $p56^{lck}$, which is associated with CD4 and CD8, thereby affecting signal transduction via these receptors (*2*). Further, the ability of the T cell antigen receptor to transduce signals leading to second messenger generation and proliferation is dependent on CD45 expression (*3*). In contrast, direct evidence for participation of CD45 in signal transduction mediated by the B cell antigen receptor has not been reported.

The plasmacytoma cell line J558Lμm3, which expresses a transfected mIgM antigen receptor (*4*), does not mobilize Ca^{2+} in response to cross-linking of that receptor (*5*). However, agents that activate GTP (guanosine triphosphate)-binding proteins, such as aluminum fluoride, do mobilize Ca^{2+} in these cells. Thus, the receptor ap-

L. B. Justement, K. S. Campbell, N. C. Chien, J. C. Cambier, Division of Basic Sciences, Department of Pediatrics, National Jewish Center for Immunology and Respiratory Medicine. J. C. Cambier, also at Department of Microbiology and Immunology, University of Colorado Health Sciences Center, Denver, CO 80206

*Present address: Department of Microbiology, J-19, The University of Texas Medical Branch, Galveston, TX 77550.

†To whom correspondence should be addressed.